Journal of Neural Engineering

PAPER

A brain-actuated robotic arm system using non-invasive hybrid brain–computer interface and shared control strategy

Linfeng Cao[1], Guangye Li[1], Yang Xu[1], Heng Zhang[1], Xiaokang Shu[1] and Dingguo Zhang[2,*]

[1] State Key Laboratory of Mechanical Systems and Vibrations, Institute of Robotics, Shanghai Jiao Tong University, Shanghai, People's Republic of China
[2] Department of Electronic and Electrical Engineering, University of Bath, Bath, United Kingdom
[*] Author to whom any correspondence should be addressed.

E-mail: d.zhang@bath.ac.uk

RECEIVED
26 November 2020

REVISED
15 April 2021

ACCEPTED FOR PUBLICATION
16 April 2021

PUBLISHED
5 May 2021

Keywords: shared control, hybrid brain–computer interface, computer vision, intention inference, Bayesian fusion, robotic arm

Supplementary material for this article is available online

Abstract

Objective. The electroencephalography (EEG)-based brain–computer interfaces (BCIs) have been used in the control of robotic arms. The performance of non-invasive BCIs may not be satisfactory due to the poor quality of EEG signals, so the shared control strategies were tried as an alternative solution. However, most of the existing shared control methods set the arbitration rules manually, which highly depended on the specific tasks and developer's experience. In this study, we proposed a novel shared control model that automatically optimized the control commands in a dynamical way based on the context in real-time control. Besides, we employed the hybrid BCI to better allocate commands with multiple functions. The system allowed non-invasive BCI users to manipulate a robotic arm moving in a three-dimensional (3D) space and complete a pick-place task of multiple objects. *Approach.* Taking the scene information obtained by computer vision as a knowledge base, a machine agent was designed to infer the user's intention and generate automatic commands. Based on the inference confidence and user's characteristic, the proposed shared control model fused the machine autonomy and human intention dynamically for robotic arm motion optimization during the online control. In addition, we introduced a hybrid BCI scheme that applied steady-state visual evoked potentials and motor imagery to the divided primary and secondary BCI interfaces to better allocate the BCI resources (e.g. decoding computing power, screen occupation) and realize the multi-dimensional control of the robotic arm. *Main results.* Eleven subjects participated in the online experiments of picking and placing five objects that scattered at different positions in a 3D workspace. The results showed that most of the subjects could control the robotic arm to complete accurate and robust picking task with an average success rate of approximately 85% under the shared control strategy, while the average success rate of placing task controlled by pure BCI was 50% approximately. *Significance.* In this paper, we proposed a novel shared controller for motion automatic optimization, together with a hybrid BCI control scheme that allocated paradigms according to the importance of commands to realize multi-dimensional and effective control of a robotic arm. Our study indicated that the shared control strategy with hybrid BCI could greatly improve the performance of the brain-actuated robotic arm system.

1. Introduction

Brain–computer interface (BCI) has enabled the human brain to directly transmit information to external device (Vallabhaneni *et al* 2005). This technology is widely considered to be a potentially effective approach to reconstruct the basic ability for paralyzed people in activities of daily living (ADL). The development of signal acquisition and decoding technologies have led to the rise of

© 2021 IOP Publishing Ltd

many brain-actuated applications including quadcopter (Wang *et al* 2018, Yan *et al* 2020), wheelchair (Tanaka *et al* 2005, Pinheiro *et al* 2018), speller output (Chen *et al* 2015b, Lin *et al* 2018) and computer operation (He *et al* 2020). Meanwhile, the brain-actuated robotic arm system, as one of the most promising and direct technologies in restoring the motor functions of the upper limbs, plays an important role in the BCI applications. Therefore, how to drive a dexterous robotic arm using BCI technology to better assist the paralyzed people in completing ADL, has always been a challenge to be addressed.

Up to the present, remarkable progress on brain-actuated robotic arm systems have been made using invasive (Hochberg *et al* 2012, Flesher *et al* 2016) and non-invasive BCI approaches (Meng *et al* 2016, Chen *et al* 2018, Xu *et al* 2019). Whereas the invasive BCIs have the limitations of surgical risk and signal degradation, the non-invasive BCI technology thus becomes a valuable way in practical application, where sensorimotor rhythms (Meng *et al* 2016, Xu *et al* 2019), steady-state visual evoked potentials (SSVEP) (Li and Zhang 2016, Han *et al* 2018, Chen *et al* 2019) and event-related potentials (Johnson *et al* 2010, Pathirage *et al* 2013) are the most widely used paradigms in non-invasive BCI robotic arm control. Despite plenty of pilot studies have been carried out (Daly and Wolpaw 2008, Onose *et al* 2012), increasing the dimensionality of control and improving the control performance are still the main topics for non-invasive BCI actuated robotic arm system.

To extend the dimension of BCI control, some studies implement motor imagery (MI) involving different combinations or different body parts (e.g. imagination of right hand, left hand, both hands and rest (Edelman *et al* 2019); imagination of finger, elbow, shoulder and hand (Bhattacharyya *et al* 2014)). Even though the MI paradigm enables more initiative BCI control, the dimensionality is still limited. As a comparison, SSVEP relies on visual stimuli but can achieve a much higher information transfer rate (ITR) than MI. In this context, hybrid BCI, which explores different combinations of BCI paradigms, such as SSVEP and MI (Gao *et al* 2017, Duan *et al* 2019), P300 and MI (Long *et al* 2011), provides more BCI outputs than any single paradigm and thus can work as a possible way to broaden the dimensionality of BCI control. One of the pioneering works of hybrid BCI was the combination of MI and P300 (responsible for horizontal and vertical movement control of cursor), which allows the user to conduct both paradigms simultaneously to control the cursor moving in the two-dimensional (2D) plane (Li *et al* 2010). Based on a similar motivation, a number of hybrid BCI studies, such as SSVEP and MI (Rakshit *et al* 2016, Gao *et al* 2017, Duan *et al* 2019), visual evoked potential and MI (Ma *et al* 2017) have been developed for motion control as well. In addition, the hybrid BCI has also been regarded as a way to counter the low performance with a given paradigm by involving others (de Neeling and Hulle 2019). Some studies have demonstrated that the implementation of hybrid BCI including P300 versus SSVEP (Wang *et al* 2015), MI versus SSVEP (Yu *et al* 2015, McGeady *et al* 2019), can improve the decoding performance upon the individual paradigm.

However, most of the existing hybrid BCI approaches for command extension only focus on the number of command while rarely take the command's usage rate and importance level for BCI resources optimization (Rakshit *et al* 2016, Gao *et al* 2017, Duan *et al* 2019). Considering that in some occasions, different control commands will inevitably have different accuracy requirements and usage rates. In this study, we first applied the hybrid BCI paradigm including MI and SSVEP to multi-dimensional control from the perspective of dividing the primary and the secondary control interfaces. Specifically, we ranked the importance of each motion command empirically according to the accuracy and calling requirements, then assigned the corresponding control paradigm for it. For the 2D plane movement and placing control (requiring high accuracy and good real-time performance), the primary interface (PI) with five-class SSVEP was implemented due to the considerable decoding accuracy and ITR. For the vertical control (relatively lower usage rate and accuracy requirement), the secondary interface (SI) was applied. With the advantage of independent generation, the MI paradigm does not require any external stimuli of graphic user interface (GUI), which is suitable for the SI. The implementation of hybrid BCI paradigm aimed to optimize the GUI redundancy (resource waste due to low usage rate of some commands) caused by using a single paradigm (e.g. pure SSVEP). For the commands with lower utilization rate, the SI (active paradigm) was utilized, which could enhance the performance of the PI and ensure the basic operation of the SI in multi-dimensional control.

Apart from the dimensionality of control, the performance of robotic arm system is another critical issue. To guarantee the system performance, the control strategy of the brain-actuated system plays an important role. Generally, the fully BCI-manipulated robotic arm system has been suffering from imprecise neural decoding (e.g. accuracy and stability), and consequently, is still inefficient in high-precision control tasks (Kim *et al* 2015, Xu *et al* 2019). Another approach, the shared control method, taking use of the involvement from both human and machine during the control process, can gain the ability of completing more complex tasks for a BCI-actuated robotic arm system (Crandall and Goodrich 2002, Bi *et al* 2013, Sun *et al* 2019). A number of studies have proven that the adoption of machine autonomy can greatly improve the performance of BCI control

(Li *et al* 2017, Kim *et al* 2019, Deng *et al* 2020, Xu *et al* 2020), as the systems take the advantage of human supervision for higher-level task planning and utilize autonomy to reliably solve high-precision tasks (Muelling *et al* 2017). Another advantage of the shared control approach lies in the learning potential of the machine autonomy in the process of human-computer cooperation. In some well-defined tasks, through a feedback (e.g. error-related potential) cycle between human and robot, the robot is constantly taught and the performance of cooperation is improved (Iturrate *et al* 2015, Kim *et al* 2017, Salazar-Gomez *et al* 2017). These studies demonstrate the human feedback during control might be useful in the future to adapt the behavior of machine autonomy to better align with human expectations without the need for explicitly programming each task (Ehrlich and Cheng 2018, Cheng *et al* 2020).

To avoid rigid control handover (Iturrate *et al* 2009, Perera *et al* 2016, Chen *et al* 2019, Xu *et al* 2019) and provide a flexible intervention of machine autonomy, we implemented the synchronous shared control mode which makes use of human real-time feedback and regulation in the control process. At present, many of the proposed shared control systems are manually set the arbitration coefficients (Li *et al* 2017, Muelling *et al* 2017, Xu *et al* 2019) or fusion rules (Sun *et al* 2019) based on the specific tasks and empiricism. Although they can enhance task performance in the given scenarios, the performance of machine autonomous assistance is limited due to the dependence on empiricism in preset parameters and poor adaptability to different scenarios. In this study, we proposed a shared controller that dynamically constructed human intention and machine autonomy probability models based on the confidence of the user intent inference and decoding accuracy of user respectively in real-time to guarantee the contextuality of arbitration, and the corrected motion command was optimized automatically using Bayesian fusion theory (Guo and Li 2008) without setting arbitration conditions in advance.

In all, the framework presented in this study incorporated a hybrid BCI scheme and a shared controller to enhance the overall capability for the brain-actuated robotic arm system. In detail, a hybrid BCI scheme based on PI and SI was adopted to realize the multi-dimensional control and optimize the BCI resource allocation. The established shared controller dynamically constructed human intention and machine autonomy probability models, and fused them using Bayesian fusion theory to optimize the robot control automatically. The system performance was tested and evaluated under the scene of a specific ADL (pick and place the desired object).

2. Material and methods

The whole platform consisted of two subsystems: BCI subsystem and robot subsystem (figure 1). The BCI subsystem was mainly responsible for GUI display, electroencephalography (EEG) signal acquisition and decoding, transmitting the intention of the human agent to the controller. The main functions of the robot subsystem were control optimization and motion execution. Within the robot subsystem, an autonomous sensing module for multi-target objects was embedded as a machine agent, which predicted the user's intention and generated autonomous command. The proposed shared controller blended the output commands from human and machine agents to provide assistance in real time control. In the following sections, we will use 'machine agent' to refer to the automatic command generator and 'robot' to refer to the hardware platform of motion execution.

2.1. BCI subsystem

2.1.1. User interface design

To realize the multi-dimensional control of the robotic arm, we ranked importance of each command according to the task in our study (pick and place the desired object, detailed in section 2.3.3) and divided the control interface into PI and SI. Specifically, a five-class SSVEP interface was implemented as PI for robot movement control in the x–y plane and autonomous place (i.e. adjusting the height and releasing the gripper automatically), while a two-class MI interface was implemented as SI for robot vertical movement control. Before the online test, an offline experiment consisted of MI and SSVEP tasks was implemented for model calibration and evaluation (detailed in section 2.3.2). The experiment protocol and GUI in the offline experiment are shown in figure 2(a). The flickering stimuli frequencies for SSVEP were 10, 11, 12, 13 and 14 Hz. To effectively evaluate the performance of hybrid BCI in practical application, five SSVEP flickering blocks would be displayed on the screen in all offline trials. The online experiment consisted of picking and placing processes (detailed in section 2.3.3). The GUI of online control is shown in figure 2(b), with four directional SSVEP blocks mapping to the robot commands of moving forward, backward, left, right, and one lower right SSVEP block as placement command during the placing process. Left-hand MI and right-hand MI were mapped to the robot vertical up and down commands. The subjects could view the real-time scene image in the center of the screen. Simultaneously, the decoded BCI result was cued through a green box on the corresponding SSVEP block or a green vertical bar indicating the MI directions (figure 2(b)).

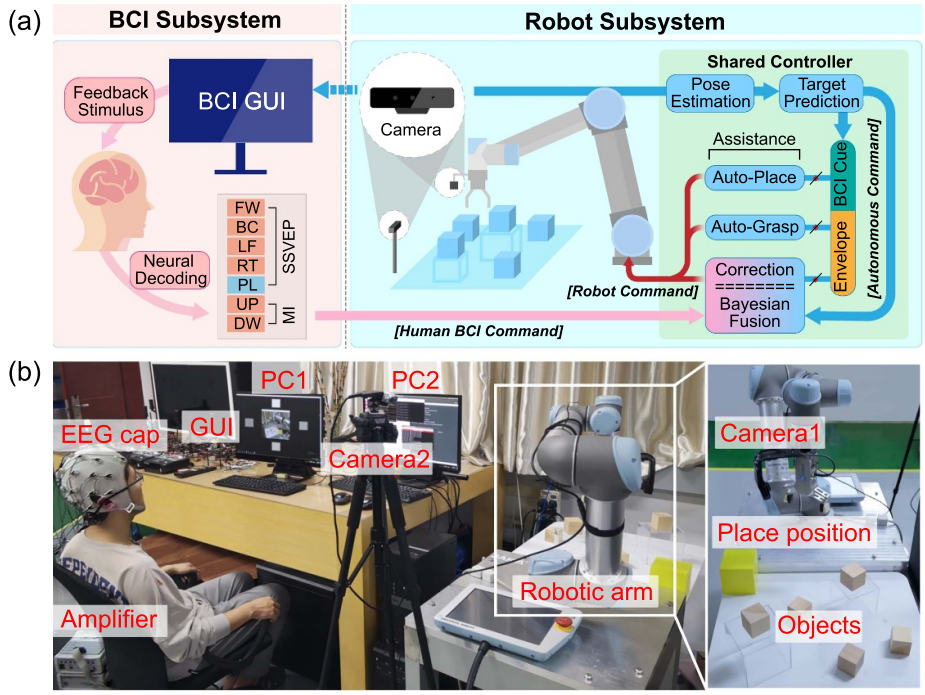

Figure 1. (a) The architecture of the brain-actuated robotic arm system. The platform consisted of BCI (left box, PC1 in subgraph b) and robot (right box, PC2 in subgraph b) subsystems. The subject executed the hybrid BCI paradigms through GUI and the identified control command was sent to the robot subsystem. The robot subsystem predicted the user's intention, generated autonomous commands and then blended human and machine agent results into robot control instructions using Bayesian fusion theory. One RGB-D camera (Camera1 in subgraph b) was fixed at the end of the robotic arm to detect the objects, whose poses would be calculated as the knowledge base for shared control. Another camera (Camera2 in subgraph b) was fixed outside the task area to transmit the real-time scene image to the GUI. (b) The experimental setup of the brain-actuated robotic arm system.

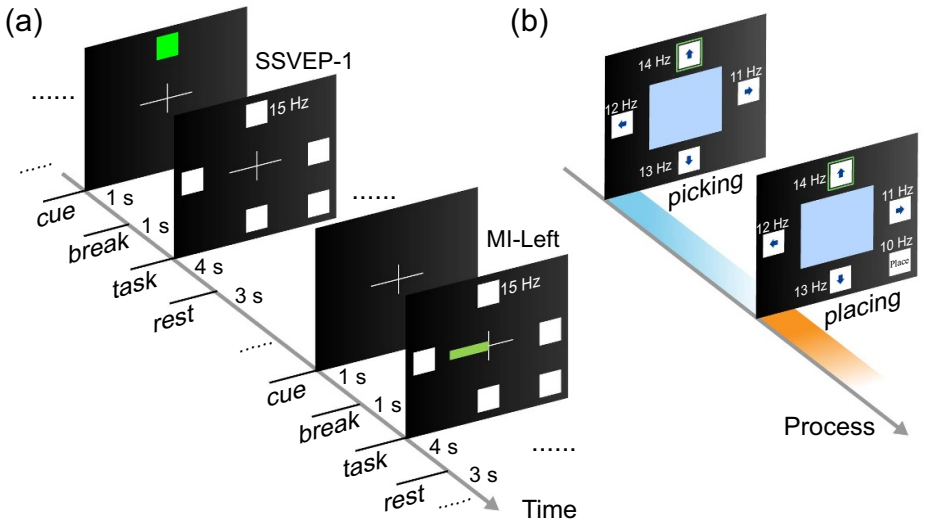

Figure 2. The user interface of the hybrid BCI and experimental protocol. (a) The user interface and protocol of offline experiment. Each participant performed 5-class SSVEP or left-, right-hand MI according to the SSVEP block cue or MI bar cue. The order was randomized. The protocol started from a 1 s cue period of SSVEP (cross with a block) or MI (cross only, direction was prompted during task period). Then there was a break period of 1 s. Next, subject was required to perform the corresponding task for 4 s. Following that was a 3 s rest period. (b) The user interface and protocol of online experiment. The online experiment consisted of picking and placing processes (detailed in section 2.3.3). There were four SSVEP blocks during the picking process for robot movement and five SSVEP blocks during the placing process for robot movement and placement.

2.1.2. Data acquisition and analysis

The EEG signals were recorded with a BrainAmp amplifier (Brain Products GmbH, Germany) using a 32-channel electrode cap. The signals were referenced to the left mastoid and sampled at 200 Hz. Fourteen electrodes (FC5, FC1, FC2, FC6, C3, Cz, C4, CP5, CP1, CP2, CP6, O1, Oz and O2) were selected for signal recording and electrode Fpz was set as the ground

Table 1. Gridding projection principles between original feature vector $\boldsymbol{F_{OR}}$ and final feature vector $\boldsymbol{F_{GN}}$.

Original value	≥8	[7, 8)	[6, 7)	[5, 6)	[4, 5)	[3, 4)	[2, 3)	[1, 2)	<1
Grid-normalization Value	1	0.9	0.8	0.7	0.6	0.5	0.3	0.2	0

channel. Following that, a Chebyshev Type I band-pass filter with a bandwidth of 6–35 Hz was applied in MATLAB for signal pre-processing, to obtain the neural activities (i.e. mu and beta rhythms between 8 and 30 Hz (Pfurtscheller and Lopes da Silva 1999), the first-order and second-order SSVEP responses). During online decoding, we called the MATLAB engine in C++ program to process the recorded EEG signal in realtime. At the decoding stage, we implemented a two-layer BCI classifier to realize the parallel control of PI and SI. The first layer was a hybrid decoder to identify the user's current BCI paradigm (SSVEP or MI). For the purpose of decoding two paradigms independently, the second layer consisted of two parallel decoders (i.e. MI decoder and SSVEP decoder respectively), whose activation was depending on the outcomes of the first layer decoder. And finally the activated one output the corresponding BCI control commands.

Considering the notable modulation of the spectrum at the occipital lobe while the subjects were receiving SSVEP stimulation (Sutter 1992), we regarded it as the crucial feature for hybrid decoding. Specifically, three channels (O1, O2, Oz) which located at the occipital area and presented the strongest SSVEP evoked responses were selected for hybrid and subsequent SSVEP classifications. Then, a fast Fourier transform (FFT) was implemented to extract the spectrum information of band-passed filtered signals. To enhance the notability of key peaks, the averaged spectrum over three channels was squared, which could further increase the gap between the key peak values and the common signal values. Then, five peak pair vectors $\boldsymbol{f}_i = [a_i, b_i]$ $(i = 1, 2, 3, 4, 5)$ were obtained by taking the amplitudes at the corresponding bands of SSVEP stimuli frequencies. Each peak pair vector $\boldsymbol{f_i}$ consisted of two maximum squared amplitudes a_i and b_i within the basic stimuli frequency second harmonic frequency bands. The peak pair vector with the maximum sum was assumed to be the strongest evoked response and was divided by the mean of the entire squared spectrum to obtain the original feature vector $\boldsymbol{F_{OR}}$:

$$I = \arg\max_i (a_i + b_i), i = 1, 2, \ldots, 5, \tag{1}$$

$$\boldsymbol{F_{OR}} = [F_1, F_2] = \frac{\boldsymbol{f}_I}{\mathrm{mean}(\textit{squared spectrum}[6, 35]\ \textit{Hz})}. \tag{2}$$

Then we performed a normalization to remap the original feature vector $\boldsymbol{F}_{OR}$ into a fixed value between 0 and 1 ($\boldsymbol{F}_{GN}$, table 1). The grid-normalized vector $\boldsymbol{F}_{GN} = [F_1, F_2]$ was subsequently sent to a linear discriminant analysis (LDA) classifier as the feature for hybrid decoding. The hybrid decoder generated the binary output to activate one of the classifiers at the second level.

As to the two parallel decoders in the second layer, for MI decoding, the common spatial pattern (CSP) algorithm (Blankertz *et al* 2007) was implemented to extract the feature vectors and LDA classifier was employed for final classification over the selected fourteen channels. For SSVEP decoding, the band filter canonical correlation analysis (FBCCA) spatial filtering was applied over three channels (O1, O2 and Oz) (Chen *et al* 2015a). The frequency of reference template which had the maximum correlation with the EEG signals was regarded as the stimulus frequency that the subjects were paying attention to. In order to ensure the robustness of online control, the output commands of FBCCA was further re-corrected by the strongest peak pair vectors obtained in the hybrid decoder. If the frequency of FBCCA decoded command was consistent with that of the peak pair vector with the maximum sum in hybrid decoder, a new SSVEP command was generated. Otherwise, the command remained unchanged from the previous control cycle (the interval duration from the last control command output to the next control command update). In the online control, the sliding window was set to be 3 s to ensure the frequency resolution of the signal. The step length was adjusted to 0.5 s according to the moving speed of the robot and the actual control performance, as a trade-off between the control sensitivity and stability.

2.2. Robot subsystem

The robot system mainly consisted of one UR5 robotic arm (Universal Robots, Denmark) equipped with an RG2 gripper (On Robot, Denmark), two RealSense SR300 RGB-D cameras (Intel Corporation, USA) and a shared controller (figure 1). The maximum action radius of the robot is 0.85 m and the gripper stroke is 0.11 m. One camera was fixed at the assembly end of the gripper to realize the eye-in-hand vision. The other camera was fixed outside the task area to transmit the real-time scene image to the BCI subsystem (see figures 1 and 2(b)). The whole robot control platform was developed in Ubuntu operating system based on the robot operating system (ROS).

2.2.1. Object recognition and pose estimation

To provide control assistance, the poses of all potential targets were estimated at the beginning of each

trial to update the knowledge base. The image and point clouds of the work area scene were captured by the RGB-D camera fixed at the end of the robot (figure 1). In this study, a fully convolutional networks (FCN) model was implemented to identify the potential targets from the captured scene image and perform semantic segmentation on them (Long *et al* 2015). For the network pretraining, we used the camera fixed at the assembly end of the gripper to capture 2000 images of the experimental scene with different objects, and utilized the deep learning annotation tool LabelMe (Russell *et al* 2008) to manually cut and label the images to build the data set (seven types of labels: background, wooden block, Oreo box, garbage bag, banana, apple and orange). As a neural network of which all layers are convolution layer, FCN recovers the category of each pixel from the abstract features, solving the problem of image segmentation at the semantic level. The performance of the pretrained model was evaluated on the test set, and the average pixel classification accuracy was 92.74% over seven categories. The error rate was mainly concentrated on the pixels of the object boundary, and had little effect on the recognition result of the objects. Due to the correspondence between the point cloud and image pixel in the same frame, the objects' point cloud could be extracted by taking the reference of the FCN output image. To estimate the object's poses, the extracted point clouds were processed based on the Point Cloud Library (Rusu and Cousins 2011). Firstly, the source point cloud was downsampled and then pass-through filtered to get a higher quality point cloud. After that, the point cloud of each object was extracted separately by the Euler clustering algorithm (Rusu and Cousins 2011, Wu *et al* 2013). It can cluster data points according to the preset Euclidean distance threshold, which is very suitable for independent segmentation and extraction of spatial point cloud clusters in different locations. Finally, the iterative closest point algorithm, a classic data registration method for solving the transformation matrix with simple principle and good accuracy, was implemented to calculate the poses of objects (Rusu and Cousins 2011). Before each online experiment, we would display the results of FCN recognition and pose estimation in the 3D visualization tool rviz of ROS to ensure the accuracy of the knowledge base for the experiment. If any online task failed due to the error of target recognition and pose estimation, it would not be recorded because it had nothing to do with the online BCI control process, and the subjects would be required to conduct the experiment again.

2.2.2. Target prediction

In the online experiment of robot control, the process of each trial could be divided into two stages: picking process and placing process (detailed in section 2.3.3). During the picking process, the intention prediction for users in real-time was introduced. The model of target prediction was established based on the maximum entropy principle which intuitively infers the probability distribution over goals using the existing information without introducing any subjective inference (Muelling *et al* 2017).

According to the motion information of the robot, we could estimate the possibility of each potential target G given its cost function C_G. In this study, we assumed that the users were always trying to minimize the cost function C_{G^*} of their intended object G_*. Using the maximum entropy principle, the probability distribution of one potential target G_i over trajectories ξ was established as $P(\xi|G_i) \propto \exp(-C_{G_i}(\xi))$ (Ziebart *et al* 2008, Muelling *et al* 2017). Considering that in the whole control loop, the user would adjust the BCI output (by attending the flickering patches and/or performing MI) in real-time according to the current context in the task, the probability distribution did not have to be calculated perfectly. Hence, we approximated $C_{G_i}(\xi)$ by its second-order Taylor series expansion (Dragan and Srinivasa 2013) and finally simplified the probability model over trajectory as:

$$P(\xi_{S\to E}|G_i) = \frac{\exp\left(-C_{Gi}\left(\xi_{S\to E}\right) - C_{Gi}\left(\xi^*_{E\to Gi}\right)\right)}{\exp\left(-C_{Gi}\left(\xi^*_{S\to Gi}\right)\right)}, \quad i = 1, 2, \ldots, 5, \tag{3}$$

where S is the start point for prediction, E represents the current location of robot end and G represents the location of object, ξ^* represents the optimal trajectory to G_i. Eventually, the probability per potential goal could be calculated by normalizing the probability distribution to sum up to 1:

$$P(G_i|\xi_{S\to E}) = Normalization\left(P(\xi_{S\to E}|G_i)\right). \tag{4}$$

In our study, the Euclidean distance between two ends of the trajectory in x–y plane was chosen as the cost function C_G. Although some trajectory details were abandoned, the advantage was that it could roughly reflect the trajectory of the robot based on current information (e.g. position) and was convenient to measure intuitively.

Due to the explosive growth of exponential function, it was necessary to preset the calculation interval of probability (equation (3)) to guarantee the rationality and stability of the target prediction results. Based on the simulation results, we finally chose [0, 15] that could achieve the most reasonable probability assignment as the numerical interval of cost function C_G (i.e. the Euclidean distance between two ends) and remapped the x–y plane of work area to that scale in the online control experiment. Considering that there would inevitably be some controversial task scenarios (e.g. some objects were in a straight line with the initial point), we took the position where the robot entered the work area as the

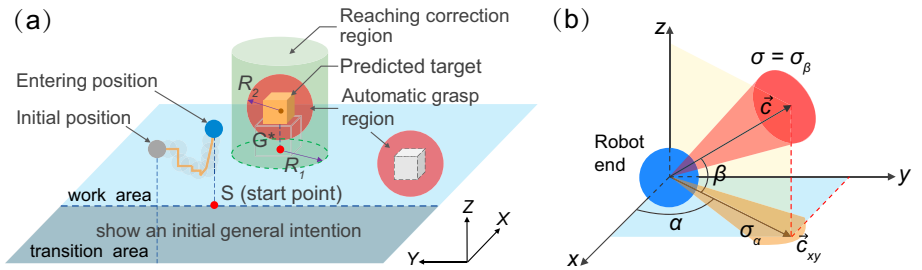

Figure 3. The strategy of shared control. (a) Stereogram of work scene. The front space is a transition area, where subjects exert their rough intention. The back area is the work area, where the machine infers the user's intention and provides assistance. The translucent green cylinder area is the reaching correction region of the predicted target and the red sphere areas are the automatic grasp regions of the objects. (b) Robot motion decomposition diagram. The blue ball represents the robot end. The red transparent cone area represents the probability model (with standard deviation σ) of the agent, while the orange area is the projection of that in $x-y$ plane.

start point of the trajectory instead of the robot initial position (figure 3(a)). Hence, the start point of each trial was not fixed. Within the transition area, subjects were required to show a general intention to the machine agent by controlling the robot to approach the desired target in the y-axis (left/right) direction via PI (SSVEP) for target preliminary screening. Once got the trajectory start point, the machine agent marked the corresponding interest area and selected two objects closest to the start point in the y-axis (left/right) direction as the potential targets. Only these two potential targets would be utilized by the machine agent in target prediction to infer the user's intention and provided reaching correction assistance for them. Nevertheless, the user could still control the robot to pick other objects automatically as long as the robot end-effector moved into their grasp envelopes, but it would no longer provide the reaching correction assistance for these objects in the process of approaching.

2.2.3. Shared control strategy

Three different shared control assist modes including reaching correction, automatic grasp and automatic place were implemented in the shared controller. During the task period, the shared controller decided whether or not to provide shared control assistance and what kind of assistance to provide, according to the current robot position and the output commands from human and machine agents.

In this case, a cylinder envelope (radius R_1: 0.1 m centered on the predicted target in x–y plane was set as the reaching correction region, and spherical envelopes (radius R_2: 0.05 m) centered at each object were set as the automatic grasp regions (figure 3(a)). When the end of the robot was outside the reaching correction region of the predicted target, the robot was completely controlled by the human agent (BCI command). After entering the reaching correction region, the machine agent provided partial traction assistance, and cooperated with human agent to control the robot to approach the target object. As long as the end of the robot entered any automatic grasp region, the machine agent took over and grasped that object automatically. When the object was grasped, the experiment went into the placing stage. During this stage, users were required to control the robot move to the predefined position (given by the task) and place the object, where the robot was controlled by human agent (BCI command) only. Once the SSVEP command of placing action was triggered (figure 2(b) and section 2.1.1), the machine agent took over again and complete the placement by adjusting the height automatically.

In detail, when reaching correction assist mode was activated, a shared control model was implemented by blending the human intention (H) and the machine autonomy (M) into the robot control command (C). Considering the potential non-discrete angle demand of humans and uncertainty from both neural decoding and machine inference, we established the probability models of human and machine agents under the current control cycle and constructed the final robot command model $F(C)$ based on the Bayesian fusion theory as follows:

$$F(C) = P(C|H,M) = \frac{P(H|C)\,P(M|C)\,P(C)}{P(H)\,P(M)} = \eta P(H|C)\,P(M|C)\,, \tag{5}$$

where $P(H|C)$ and $P(M|C)$ represent human intention and machine autonomy probability models respectively. $P(H)$ and $P(M)$ are prior probabilities of human intention and machine autonomy. Due to the arbitrary direction of movement for the dexterous robotic arm in each control cycle, the desired outputs of two agents in each control cycle were independent of each other. Thus the prior probabilities of H, M, and C were uniform distributions at each control cycle and could be simplified as constant parameters. η is a constant value used for normalization. In this study, both the human intention model and the machine autonomy model were assumed to obey Gaussian distributions:

$$\begin{cases} P(H|C) = \frac{1}{\sigma_H\sqrt{2\pi}}\exp\left(-\frac{(c-c_H)^2}{2{\sigma_H}^2}\right) \\ {\sigma_H}^2 = 1+\exp\left(-k\times p_{BCI}\right) \end{cases} \tag{6}$$

$$\begin{cases} P(M|C) = \frac{1}{\sigma_M\sqrt{2\pi}}\exp\left(-\frac{(c-c_M)^2}{2{\sigma_H}^2}\right) \\ {\sigma_M}^2 = 1+\exp\left(-k\times p_{pre\_target}\right) \end{cases}, \tag{7}$$

where c_H is the BCI decoded command, c_M is the machine autonomous command, whose direction was from the current robot end to the centroid of the predicted target. They represent the expected values in $P(H|C)$ and $P(M|C)$ (equations (6) and (7)). The variances ${\sigma_H}^2$ and ${\sigma_M}^2$ are determined by the confidences of their corresponding commands. $k>0$ is a constant for variance adjustment. p_{BCI} is the product of average offline hybrid BCI and MI or SSVEP decoding accuracy rate. p_{pre_target} is the inferred target probability obtained by the target prediction model (equation (4)).

To calculate the control vector distributions in the 3D workspace, we decomposed the variable vector $\boldsymbol{c}$ (equations (6) and (7)) into two parameters: α). the angle between the projection of motion vector in x–y plane ($\boldsymbol{c_{xy}}$) and x-axis; β). the angle between motion vector $\boldsymbol{c}$ and x–y plane. The robot end coordinate is shown in figure 3(b). Hence the models of human intention and machine autonomy were two-dimensional Gaussian distributions based on α and β:

$$\begin{cases} P(H|C) \\ or \\ P(M|C) \end{cases} = f(\alpha,\beta) = \frac{1}{2\pi\sigma_\alpha\sigma_\beta\sqrt{1-\rho^2}} \times\exp\left[-\frac{1}{2(1-\rho^2)}\left(\frac{(\alpha-\alpha')^2}{{\sigma_\alpha}^2}-\frac{2\rho(\alpha-\alpha')(\beta-\beta')}{\sigma_\alpha\sigma_\beta}+\frac{(\beta-\beta')^2}{{\sigma_\beta}^2}\right)\right], \tag{8}$$

where α' and β' are the decomposed angles of BCI decoded or autonomous command vector; ${\sigma_\alpha}^2$ and ${\sigma_\beta}^2$ are the decomposed variances of σ_H or σ_M; ρ is the correlation coefficient between α and β. Considering α and β are two independent parameters of the robot motion vector, the correlation coefficient is 0. Hence, the command model can be simplified as:

$$\begin{aligned} f(\alpha,\beta) &= \frac{1}{2\pi\sigma_\alpha\sigma_\beta} \times\exp\left[-\frac{1}{2}\left(\frac{(\alpha-\alpha')^2}{{\sigma_\alpha}^2}+\frac{(\beta-\beta')^2}{{\sigma_\beta}^2}\right)\right] \\ &= f(\alpha)f(\beta). \end{aligned} \tag{9}$$

The final robot control command model could be constructed as:

$$\begin{aligned} F(C) &\propto P(H|C)P(M|C) \\ &= f(\alpha_H,\beta_H)f(\alpha_M,\beta_M) \\ &= f(\alpha_H)f(\beta_H)f(\alpha_M)f(\beta_M) \\ &= [f(\alpha_H)f(\alpha_M)][f(\beta_H)f(\beta_M)]. \end{aligned} \tag{10}$$

The α and β distributions of human intention or machine autonomy could be expressed as:

$$\begin{cases} f(\alpha) = \frac{1}{\sigma_\alpha\sqrt{2\pi}}\exp\left(-\frac{(\alpha-\alpha')^2}{2{\sigma_\alpha}^2}\right) \\ \sigma_\alpha = \tan^{-1}\left(\frac{\tan\sigma}{\cos\beta}\right) \end{cases} \tag{11}$$

$$\begin{cases} f(\beta) = \frac{1}{\sigma_\beta\sqrt{2\pi}}\exp\left(-\frac{(\beta-\beta')^2}{2{\sigma_\beta}^2}\right) \\ \sigma_\beta = \sigma \end{cases} \tag{12}$$

where σ represents the standard deviation of these two models in 3D space (σ_H or σ_M, shown as the red cone in figure 3(b). σ_α is the projection of σ in x–y plane (shown as the orange cone in figure 3(b), which is calculated with a geometric transform approximation. Hence, at each control cycle, the two optimal angular parameters could be calculated as below:

$$\begin{cases} \alpha_C = \arg\max_\alpha\left(f(\alpha_M)f(\alpha_H)\right) = \frac{1}{2\pi\sigma_{\alpha_M}\sigma_{\alpha_H}}\exp\left(-\frac{(\alpha-\alpha_M)^2}{2{\sigma_{\alpha_M}}^2}-\frac{(\alpha-\alpha_H)^2}{2{\sigma_{\alpha_H}}^2}\right) \\ \beta_C = \arg\max_\beta\left(f(\beta_M)f(\beta_H)\right) = \frac{1}{2\pi\sigma_{\beta_M}\sigma_{\beta_H}}\exp\left(-\frac{(\beta-\beta_M)^2}{2{\sigma_{\beta_M}}^2}-\frac{(\beta-\beta_H)^2}{2{\sigma_{\beta_H}}^2}\right) \end{cases}, \tag{13}$$

where α_C and β_C are the optimized control angels by fusing human intention with machine autonomy and will be utilized for robot control in the current control cycle.

2.3. Experiments

In this study, offline experiment and online experiment were designed and conducted with the recruited subjects respectively. The main purposes of the offline experiment were to calibrate the BCI decoder, establish the shared controller model and evaluate the performance and reliability of the user's control under this hybrid scheme, while the online experiment was to evaluate the actual control performance of this system in ADL.

2.3.1. Subjects

Eleven healthy and able-bodied subjects (average age: 23.8 ± 1.2 years, all right handed, nine males) with normal or corrected-to-normal vision were recruited in our experiment. All of the subjects had no prior experience with hybrid BCI experiment. The study was approved by the Ethics Committee of Shanghai Jiao Tong University, China (ID: ML2020036). All subjects were fully informed and signed written consent.

2.3.2. Offline experiment

During the offline calibration stage, subjects were seated on a comfortable seat, faced the screen (figure 1(b)) and were required to complete a hybrid BCI offline experiment which consisted of five-class SSVEP tasks and two-class MI tasks (left- and right-hand MI). The offline calibration consisted of two sessions with a total of 80 trials (8 trials for each SSVEP class and 20 trials for each MI class). Each trial lasted for 9 s and the order was randomized. The protocol (figure 2(a)) started from a 1 s cue period of SSVEP (cross with a prompted block) or MI (cross only, direction was prompted during task period). Then there was a break period of 1 s, within which the subjects were required to shift their gaze to the prompted SSVEP block or focus on the screen center for the MI preparation. Afterwards, all stimuli started to flicker and the subjects were asked to perform the corresponding task as the cue indicated for 4 s. Following that was a 3 s rest period. Between two sessions, subjects could take a rest for several minutes to avoid fatigue.

The recorded data would be employed to calibrate the BCI decoder, and the offline decoding accuracy would be utilized to construct the BCI intention model. The offline accuracy of SSVEP was calculated based on the 40 SSVEP trials because no training set was needed. The decoding accuracy rates of hybrid and MI were calculated with 10-fold cross-validation.

To evaluate the performance of hybrid decoder, hybrid feature vectors distribution and time-frequency map of offline data were analyzed. Time-frequency decomposition of each trial for typical electrodes (C3, C4, Oz) was undertaken in the frequency band between [8, 30] Hz by using the decomposition functionality (FFTs and Hanning window tapering) of EEGLAB (Delorme and Makeig 2004). The final time-frequency spectrum values were calculated by grand-averaging across the trials in each mental task and then subtracting the mean value in baseline, where the task period was defined as 0–4 s and the baseline period was set as the interval from −1 to 0 s prior to the task period.

To further assess the impact of the continuous flickering SSVEP blocks on MI task execution, another additional experiment that consisted of pure left-hand (20 trials) and right-hand (20 trials) offline MI tasks was implemented on two subjects (S1 and S9). Using the acquired data, we conducted the grand-average time-frequency analysis additionally across all trials of two subjects and normalized the time-frequency spectrum to make a comparison between pure-MI and hybrid-MI. Specifically, we subtracting and dividing the spectrum value by the mean value of the baseline interval (−1 to 0 s), which could improve the phenomenon of unstable signal drift and more intuitively reflected the percentage of brain activity changes during task period compared with the baseline period.

2.3.3. Online experiment

In the online experiment, the subjects were seated on a comfortable seat, faced the screen (figure 1(b)) and were required to manipulate the robotic arm to pick one of the five objects with the assistance of shared control (picking process) and place it at the predefined position (figure 4, given by the task) using pure BCI (placing process). The design of the experiment was to simulate the action in actual life as much as possible and give a more objective evaluation on the performance of the proposed system. Specifically, considering that the position to be placed in real life was decided by the users, which was unknown for the machine (unlike the picking task), the robot was completely controlled by the discrete BCI commands during the placement process. In order to avoid the unexpected trigger of placement command caused by decoding error and enhance the robustness of placement action, the robot would only execute the motion after receiving four consecutive BCI placement commands. This parameter was determined by considering both accuracy and efficiency in the preparatory experiment evaluation.

The whole online experiment consisted of two sessions: the fixed-position session (session 1) and the random-position session (session 2). In session 1, five objects were located at the fixed locations with random poses (figure 4(a)) and two runs of pick-grasp for each object were required (i.e. 10 runs in total). In session 2, five objects were randomly arranged within

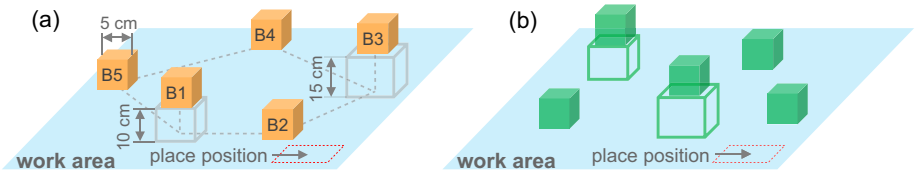

Figure 4. Distribution of objects in the online experiment. (a) Fixed-position session (session 1). (b) Random-position session (session 2).

the task area and two of them were assigned at different heights (figure 4(b)). For each of the five objects, two different random placement were applied, resulting in a total of 10 runs for this session as well. To avoid fatigue, there was an approximate 2 min rest every five runs.

Through the online experiment, the performance of the system was evaluated using a series of metrics including success rate, trajectory efficiency rate (*TER*), place distance error and completion time. Moreover, as a part of the system evaluation, after the online experiment, the workloads of picking and placing processes were assessed additionally by asking the subjects to complete a NASA-TLX (Task Load Index) questionnaire (Hart and Staveland 1988). Each index was defined in detail as below:

(a) Any trials in which the robot picked the undesired object or caused some collisions were marked as a failure. Once the robot picked the correct object, it would be marked as picking success and could be further regarded as a placing success if the robot placed the object at the predefined position (figure 4, given by the task).

(b) For the successful picking trials, we recorded the robot trajectories during the whole process. To evaluate the false positive and control efficiency, a trajectory efficiency rate (*TER*) was introduced as follows:

$$\text{Picking Process: } \begin{cases} TER_{pick_{xy}} = \frac{D_{IG_x}+D_{IG_y}}{L_{IG_x}+L_{IG_y}} \\ TER_{pick_z} = \frac{D_{IG_z}}{L_{IG_z}} \end{cases} \quad (14)$$

$$\text{Placing Process : } \begin{cases} TER_{place_{xy}} = p\frac{D_{G'P_x}+D_{G'P_y}}{L_{G'P_x}+L_{G'P_y}} \\ TER_{place_z} = p\frac{D_{G'P_z}}{L_{G'P_z}} \\ p = \frac{D_{G'P_x}+D_{G'P_y}}{D_{G'P_x}+D_{G'P_y}+D_{PC_x}+D_{PC_y}} \end{cases}, \quad (15)$$

where TER_{pick} and TER_{place} represent the efficiency rates of the picking process and placing process respectively. Subscript *IG* represents the initial start point to the grasp point, $G'P$ is the start point of the second process to the actual place point, *PC* is the actual place point to the center of the predefined place position (figure 5). *D* is the vector length between two points in x, y, z directions, while *L* is the trajectory length between two points. Since it was impossible to place the object in the designated position center perfectly in each trial, we introduced a parameter of path completion rate (p) to revise the original *TER* in the second (placing) process.

(c) To evaluate the efficiency of the system, the placement distance error index was introduced to calculate the distance between the actual placed location and the center of predefined location in the x–y plane during successful picking trials. In addition, the time of the picking process for successful picking trials (from the initial movement moment to the grasp completion moment) and the whole process time for the successful placing trials (from the initial movement moment to the placement completion moment) were recorded as completion time.

(d) The NASA-TLX is a multi-dimensional assessment that gives an overall workload score by weighted averaging ratings of six subscales: mental demand, physical demand, temporal demand, performance, effort and frustration (Hart and Staveland 1988). The subjects were asked to assess the workloads during picking and placing processes respectively. The questionnaire consisted of two procedures. The first part was to get numerical scores of each scale that revealed its level in the control process (Hart and Staveland 1988). The second part required subjects to pick out the member with greater contribution to the workload from each two-scale pair (15 possible pair-wise comparisons of six scales), thus obtained the weight (number of times selected) of each scale. The adjusted rating of each scale was calculated by multiplying its raw rating with weight. The final overall workload (OW) score during the process was obtained by summing the adjusted rating of six scales and dividing it by 15.

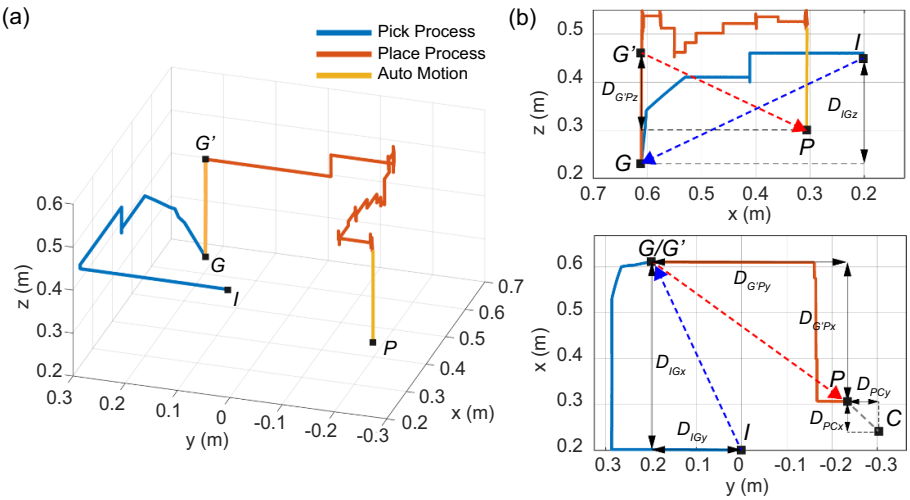

Figure 5. (a) Trajectory example of one successful trial in both picking and placing performed by subject S3. (b) Illustration of calculation intervals of TER_{pick} and TER_{place}. (I: initial start point; G: grasp position; G′: start point of placing process; P: actual place point; C: center of the predefined place position in x–y plane; The blue line represents the trajectory during the picking process; the red line represents the trajectory during the placing process and the orange line represents the automatic motion trajectory.)

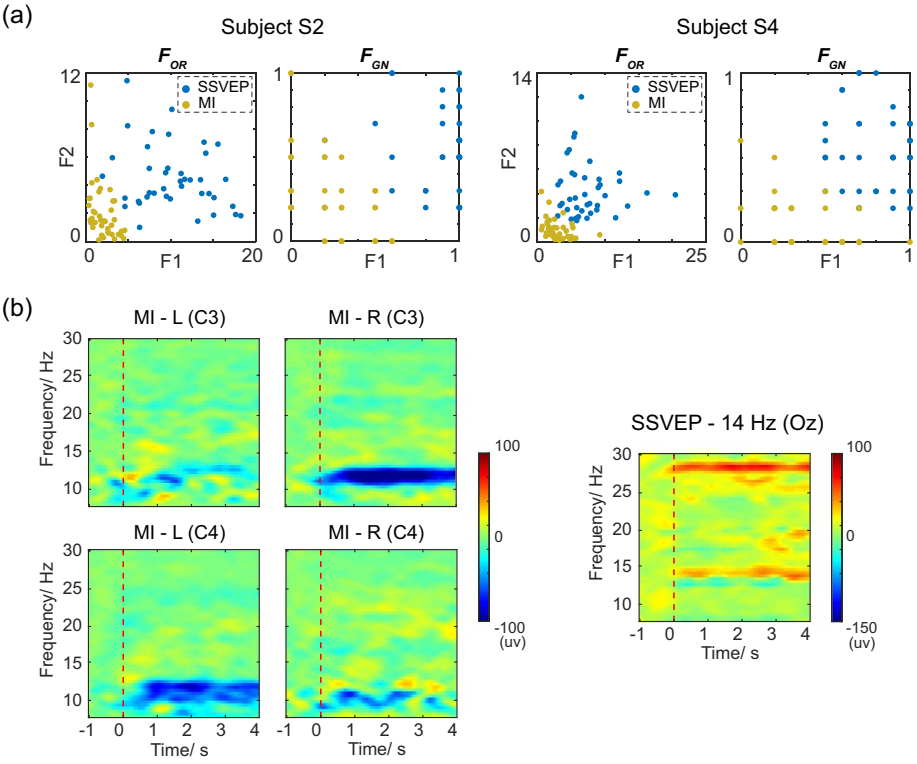

Figure 6. The visualization of EEG activities and features in the offline test from three subjects. (a) The distribution of original feature vector $\boldsymbol{F_{OR}}$ and grid-normalized feature vector $\boldsymbol{F_{GD}}$ extracted from subjects S2 and S4. (b) Grand-averaged spectrum across time and frequency domains from subject S1 (during left-hand MI, right-hand MI and 14 Hz SSVEP paradigms at C3, C4 and Oz channels respectively). Time intervals of −1 to 0 s and 0–4 s in the figure correspond to the baseline and task periods. The red dashed line indicates the onset of the task period.

3. Results

3.1. Offline results and evaluation

3.1.1. Evaluation of hybrid decoder (first layer decoder) To assess the offline performance of hybrid decoder, we evaluated the distribution of hybrid feature vectors $\boldsymbol{F_{OR}}$ and $\boldsymbol{F_{GN}}$ of each subject. Figure 6(a) shows the feature vector samples from two subjects (S2 and S4). The feature vectors of SSVEP task data tended to be larger in both dimensions (F_1 and F_2), while MI was the opposite, which suggested the difference between MI and SSVEP paradigms over the spectrum

Table 2. Offline accuracy under the hybrid BCI scheme of 11 subjects.

Subjects	Hybrid (%)	SSVEP (%)	MI (%)
S1	91.7	97.5	87.2
S2	95.2	95.0	71.7
S3	90.3	92.5	60.5
S4	87.1	87.5	72.2
S5	78.3	80.0	66.7
S6	80.8	95.0	69.0
S7	92.1	97.5	59.7
S8	81.0	75.0	71.2
S9	92.8	95.0	78.2
S10	83.3	82.5	65.7
S11	79.3	72.5	73.5
Average	86.5 ± 6.1	88.1 ± 9.2	70.5 ± 7.7

and confirmed our previous hypothesis: it was feasible to classify hybrid BCI paradigms using spectrum notability.

The offline hybrid decoding result of 11 subjects is shown in table 2 (see methods, section 2.3.2 for calculation details). For hybrid decoding, most of the subjects achieved satisfying results with an average accuracy of $86.5 \pm 6.1\%$ (mean $\pm$ SD) and the highest accuracy at 95.2% (S2). The decoding result of all subjects was above the sample size adjusted chance-level: 58.7%, $p < 0.05$ (Combrisson and Jerbi 2015).

3.1.2. Evaluation of SSVEP and MI decoder (second layer decoder)

We analyzed the signal quality in MI and SSVEP paradigms separately. Figure 6(b) presents examples of time-frequency decomposition results from subject S1 at three typical electrodes (C4, C3 and OZ), under the left-hand MI, right-hand MI and SSVEP (14 Hz) paradigms respectively. Notable task-related neural modulation for each single BCI paradigm could be seen from the figure under the hybrid scheme. The consistency between EEG activities and physiological knowledge revealed that the proposed hybrid scheme was reliable for classification and online control.

The offline decoding accuracies of SSVEP and MI over 11 subjects are shown in table 2 (see methods, section 2.3.2 for calculation details). For SSVEP decoding, most of subjects could get a good result with an average accuracy of $88.1 \pm 9.2\%$ (sample size adjusted chance-level: 32.5%, $p<0.05$) and the highest accuracy at 97.5% (S1). While the accuracy of the MI decoder was relatively lower with $70.5 \pm 7.7\%$ and two subjects' results did not exceed the sample size adjusted chance-level: 62.5%, $p < 0.05$.

3.1.3. Comparisons between hybrid-MI and pure-MI

To further assess the impact of the continuous flickering SSVEP blocks on MI task execution, an additional experiment of pure offline MI task was implemented (see methods, section 2.3.2). As could be seen from the normalized time-frequency results (figure 7), notable contralateral event-related desynchronization (ERD) was observed in both hybrid-MI and pure-MI tasks. This comparison result revealed that the intuitive and distinguishable EEG activities was also observed during hybrid-MI tasks in some key electrodes and showed a similar tendency with that in pure-MI tasks, which further indicated the feasibility of the hybrid BCI scheme.

3.2. Online experimental results and evaluation

3.2.1. Online success rate

In order to preliminarily evaluate the online performance of the brain-actuated robotic arm system, the success rate was calculated. In general, during the picking process, all subjects were capable to pick the desired objects with the assistance of the shared controller. The average success rates of picking in session 1 (fixed-position) and session 2 (random-position) were $87.27 \pm 16.18\%$ (mean $\pm$ SD) and $81.82 \pm 8.74\%$ respectively (figure 8). In the placing process, 10 of 11 subjects succeeded in placing objects at the predefined position. The success rates of placing in sessions 1 and 2 were $52.73 \pm 11.68\%$ and $48.18 \pm 10.16\%$ respectively. The obvious difference of average success rate between picking and placing process ($\sim$35%) indicated that the introduction of the shared controller could greatly improve the task performance.

Also, the smaller standard deviation during the picking process suggested that the reach correction and auto-grasp provided by the shared controller made the control procedure more robust. Moreover, there is no significant difference in the success rate between session 1 and session 2 ($p = 0.2374$ between two picking processes, $p = 0.4241$ between two placing processes; paired t-tests), suggesting that the distribution of objects had little effect on the performance.

3.2.2. Trajectory analysis

Trajectories of successful trials were recorded. Figure 5(a) shows a trajectory example of one trial succeeded in both picking and placing performed by subject S3. To evaluate the efficiency in real-time control, the index *TER* was calculated in each picking success trial (see methods, section 2.3.3). As presented in figure 9, the average *TER*s of session 1 (fixed-position) during picking and placing process in x–y plane (TER_{xy}) were $71.39 \pm 15.83\%$ and $51.12 \pm 29.09\%$ respectively, while in z axis (TER_z) were $49.10 \pm 19.79\%$ and $18.83 \pm 10.8\%$. In session 2 (random-position), with similar results to those in session 1, the TER_{xy} were $68.91 \pm 14.84\%$ and $51.25 \pm 25.12\%$ in picking and placing process, and the TER_z were $44.94 \pm 16.05\%$ and $19.88 \pm 13.11\%$ respectively. Overall, under the shared control, the average value of $TER_{pick_{xy}}$ in two sessions was about 70%, where the maximum reached 98.10%.

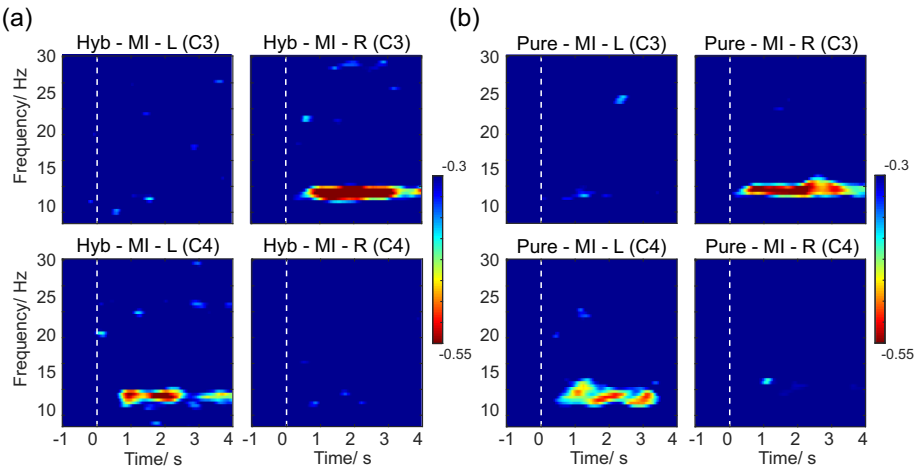

Figure 7. Grand-averaged time-frequency spectrum across subjects S1 and S9 during two paradigms. (a) Normalized time-frequency spectrum during left-hand and right-hand hybrid-MI tasks at C3 and C4 electrodes. The white dash line indicates the onset of the task period. (b) Normalized time-frequency spectrum during pure-MI tasks.

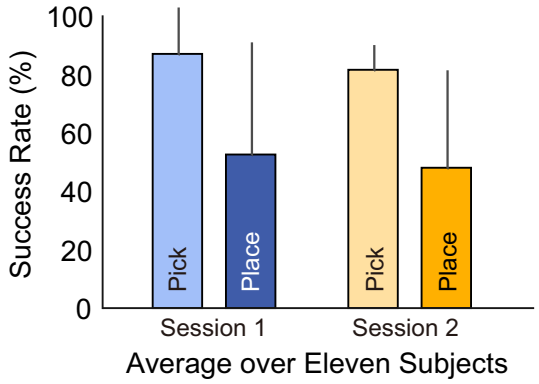

Figure 8. Success rate of online experiment in session 1 (fixed-position) and session 2 (random-position). The lighter color in each bar indicates the success rate of picking (shared control), while the darker color indicates the success rate of placing task (pure BCI control). The errorbar represents the standard deviation. (For detailed results of each individual, the reader is referred to supplementary figure 1.)

Compared with TER_{xy}, the metric of TER_z was relatively lower. There could be two reasons for this. Firstly, the sliding window was judged as an SSVEP paradigm only when the notable spectrum occurred, while the rest were judged as MI. It guaranteed the reliability of SSVEP as the PI but could affect the discrimination of MI to a certain extent (e.g. during command switching state, attention drift). Secondly, the decoding accuracy of MI was relatively lower.

Notably, similar to the results of success rate, there was also a decline of *TER* from the picking process to the placing process over two sessions. Although the starting and ending points were different in two processes and the index TER_{place} was corrected by path completion rate p, the huge decline between picking and placing process (18.92% decline in x–y and 27.67% decline in z) revealed that the reach correction and auto-grasp provided by shared controller were helpful to reduce the redundancy of robot control and further improve the task performance.

3.2.3. Completion time and place distance error

The average consuming time and distance errors are presented in figure 10(a), with an average pick time of 53.60 ± 17.20 s and an average place time of 97.20 ± 17.40 s. To adapt to the control ability of most subjects and avoid the sense of urgency, the moving speed of the robot was set to 0.03 m s^{-1}. That speed could be increased for the subjects who had good offline performance or had been well-trained, which would further shorten the consuming time in subsequent use. The average distance errors were 0.1391 ± 0.1107 m over two sessions, revealing that without the assistance provided by the shared controller, it was difficult to control the robot moving to a specified location. There were no significant differences between sessions 1 and 2 ($p = 0.7131$, 0.8010, 0.8875 among picking time, the whole task time and place distance; paired t-tests), which also reflected that the robot system had good adaptability under different scenes. Meanwhile, the smaller standard deviation of three indicators in session 2, which might be because the subjects were familiar with the robot system and control strategy after the practice, also suggested that BCI control performance of this system could be improved through continuous practice.

3.2.4. Workload assessment

The Task Load Index (TLX) analysis results over all subjects are shown in figure 10(b). The left subgraph of figure 10(b) presents the average adjusted (weighted) rating of six subscales during picking and placing processes, and the right subgraph presents the

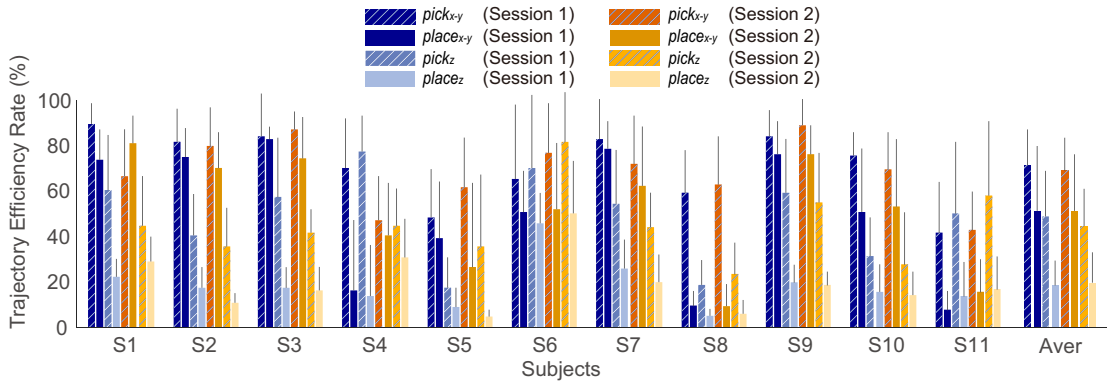

Figure 9. Trajectory efficiency rate (TER) of success trials. The purple bars represent the *TER* in session 1 (fixed-position), while the orange bars represent *TER* in session 2 (random-position). The errorbar represents the standard deviation.

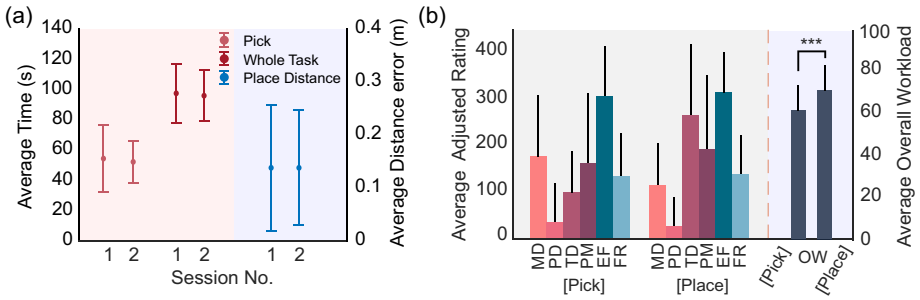

Figure 10. Task general performance and subject Task Load Index (TLX) analysis results. (a) Average completion time and place distance error of session 1 and session 2. The means and standard deviations of the completion time are plotted in the pink area, while the distance error is plotted in the blue area. (b) TLX analysis over 11 subjects. The left subgraph presents the average adjusted (weighted) rating of six subscales during picking and placing processes (MD: mental demand; PD: physical demand; TD: temporal demand; PM: performance; EF: effort; FR: frustration). The adjusted (weighted) rating of each subscale is equal to the product of its weight and raw rating. The right subgraph presents the average overall workload (OW) of picking and placing processes over 11 subjects (***$p < 0.005$; paired t-tests). The errorbar represents the standard deviation. (For detailed TLX evaluation results of each subject, the reader is referred to supplementary figure 2.)

average overall workload of picking and placing processes over 11 subjects. First of all, there was a significant difference in the overall workload between picking and placing processes ($p = 0.0012$, paired t-tests), indicating that the shared control could obviously reduce the subject's overall workload. The adjusted (weighted) rating distribution in the left subgraph revealed the contribution of each subscale to the final overall workload. During the picking process, the mental demand and effort (concentration) scored the highest among six subscales, indicating that the picking process had great demand for these two scales, especially effort (concentration). For the placing process, there were some differences: effort still ranked the first, and temporal demand ranked the second. Most of the subjects believed that the placing procedure had a certain temporal demand, but it had little influence on the workload during the picking process. It could be due to the intervention of the shared controller, which provided corresponding assistance for the high-precision motions, thus relieving the pressure of time. Although most of the subjects thought they had a good performance during tests, they still believed that good or bad performance would add to the mental burden and have a feedback effect on the subsequent control process. The adjusted rating distribution of two processes also presented the unneglectable contribution of performance and frustration, suggesting that the emotional changes caused by task performance would form feedback and further burden the subjects.

4. Discussion

Due to the inherent limitations on signal quality from non-invasive EEG, there is still plenty of room for improvement in the current EEG-based BCI targeting multi-dimensional and robust control of the dexterous robot. In this study, we proposed a brain-actuated robotic arm system, adopted with a hybrid BCI scheme based on two divided interfaces (PI, SI) and shared controller, aiming to realize the multi-dimensional control, thus providing a solution for the paralyzed people to perform specific ADL. The experiment results proved the feasibility of this system in controlling the robotic arm in 3D space and the possibility of completing a daily pick-place tasks.

Notably, the performance with shared control outperformed pure BCI control.

4.1. Multi-dimensional control and BCI resources allocation

In a complex task, there will inevitably be a variety of control commands with different usage rates and accuracy requirements. In some occasions, it may not be omnipotent to simply use one paradigm (e.g. stack stimulus blocks) to achieve multi-dimensional control. To a certain extent, it is a waste of resources to use the same paradigm control for the commands that are not commonly used or have low precision requirements in tasks, because they will constantly occupy the stimuli (GUI space) and decoding resources of the paradigm. In the proposed scheme, we divided the control interface into two levels (i.e. PI and SI), and applied hybrid BCI with SSVEP and MI on them respectively. In some task scenarios where the number of decoding command is large and the utilization of them varies greatly, the implementation of hybrid BCI based on the divided interfaces may serve as a new solution, which helps to allocate resources more reasonably and improves the performance of the main functions of the system under the limited decoding ability and command mapping conditions.

Another approach to broaden the dimensionality of control with limited command mapping and decoding ability is the repetition command mapping such as dynamic hierarchical control architecture (Han *et al* 2018) or motion decomposition (Meng *et al* 2016), which maps the same paradigm to different commands at different task stages. Compared with it, the proposed hybrid BCI scheme for multi-dimensional control in this paper has two main advantages: intuitive control logic and simple GUI design. By dividing the interface, the stimuli number of PI is reduced as much as possible to simplify the GUI. Without dynamic control mechanisms or commands remapping during tasks, the control logic is intuitive and simple. Also, the fluency of robot movement and the flexibility of control process are guaranteed.

The key to the hybrid BCI is that the signal components of each paradigm should be independent and distinguishable (Long *et al* 2011, Ma *et al* 2017). From the offline results, most of the subjects could achieve an acceptable offline performance, with $86.5 \pm 6.1\%$ accuracy for parallel hybrid decoding, $88.1 \pm 9.2\%$ for SSVEP and $70.5 \pm 7.7\%$ for MI. As shown in (figures 6 and 7), the ERDs of MI were notably revealed in both the single and hybrid MI tasks. Also, the evoked first-order and second-order responses of SSVEP could be clearly observed. All these results consistently demonstrated the feasibility of the proposed hybrid BCI scheme.

The results of online experiment revealed that the decoding accuracy of SSVEP played a decisive role in task performance. As the success rate shown in supplementary figure 1 (available online at stacks.iop.org/JNE/18/046045/mmedia), the subjects (S4, S5, S8, S11) with lower SSVEP accuracy also had a poor performance in the online experiment. On the contrary, the subjects (S3 and S7) who had the poorest MI performance, could still achieve a good success rate in the tests, as the MI paradigm (SI) was mainly responsible for dealing with some special conditions such as helping the robot get into the auto-grasp zone (when the target preliminary screening result was wrong), crossing over the undesired target if necessary. These results demonstrated the importance of SSVEP as PI in the online experiment, which were consistent with the design concept of hybrid scheme based on divided interfaces. In this study, the sliding windows were judged as the SSVEP paradigm only when a notable spectrum occurred, while the rest were judged as MI. This kind of either or decision led to false positive output of SI (e.g. during command switching state, attention drift). In the future work, a more advanced hybrid decoding method (decoding each independent paradigm component simultaneously) may improve the false positive problem of SI. Furthermore, a hybrid BCI system allowing to perform and output multi-paradigm commands simultaneously should be a better solution as to provide a more flexible control (Long *et al* 2011, Ma *et al* 2017). As an open issue, the large variability among subjects has been reported in various studies including SSVEP (Martinez *et al* 2007), P300 (Sellers *et al* 2006) and MI (Guger *et al* 2000). The results of experiment in this study also revealed the individual variability of BCI, that some subjects could complete all the tasks, while some subjects could not complete any of them. The resource priority of PI further widened the performance gap of subjects with different SSVEP accuracies in online control. A more adaptive hybrid system which can customize the control paradigms for the dividing interfaces according to the user's BCI performance, may help to improve the poor adaptability of the system due to the individual variability. Some studies have also reported to utilized the hybrid BCI to eliminate the limitation of BCI illiteracy and enhance the performance (Wang *et al* 2015, Yao *et al* 2017). Hence, applying the customized hybrid paradigm based on the dividing interfaces to give full play to the BCI ability of each subject should be a more ideal fashion to be utilized in the future. Inevitably, the multi-paradigm control will introduce some extra workload. Due to the different usage rates of PI and SI, the subjects did not switch between the two paradigms very frequently, which alleviated the pressure of multi-paradigm control to a certain extent. But the extra workload and system's complexity are still the obstacles for hybrid BCI application and need to be considered in the future.

4.2. Influence of shared controller in process control

To enhance the performance of the brain-actuated system, the auxiliary strategy of machine autonomy is another important topic. There is always a trade-off between human and machine agents in the shared control process. In our system, by blending the human intention and machine autonomy using the probabilistic method (i.e. Bayesian fusion), a dynamic balance between human and machine agents was established during the online experiment. The online evaluation results (figures 8 and 9) demonstrated that the performance in picking process (shared control) outperformed that in placing process (pure BCI control), revealing the huge improvement of ADL performance under the cooperation of human and machine intelligence.

To provide a flexible intervention of machine autonomy, we implemented the synchronous shared control mode which makes use of human real-time feedback and regulation in the control process, instead of a rigid control handover (Iturrate *et al* 2009, Perera *et al* 2016, Chen *et al* 2019, Xu *et al* 2019). For grasp execution, the autonomous grasp motion was activated once the robot got into the auto-grasp envelope of the predicted target. There is no additional confirmation (e.g. command (Chen *et al* 2018, Han *et al* 2018, Ke *et al* 2020), hovering time (Meng *et al* 2016)), which simplifies the procedure and is more similar to a natural picking process of human. The completion results also indicated the effectiveness of this method, that the confirmation confidence of target came from the whole process control, not merely the last few commands or actions.

The accuracy of BCI decoding (specially PI) is also the key to determine whether the shared controller can provide accurate assistance. Too many BCI output errors will confuse the machine agent or even lead the shared controller to make wrong assistant decisions. During the collaboration between human and autonomy, the error decision of either side will increase the difficulty of control. From the failure cases, we found that if the initial prediction point completed by the subject was unreasonable and the robot had entered into the wrong correction envelope, it was difficult to get rid of the wrong target. It may be due to the higher confidence coefficient, which gave the machine agent higher control authority after approaching the target in the later stage, making the error information previously transmitted by the subjects unable to be corrected. In addition to enhancing the BCI accuracy of human agent at the source, improving the capabilities of error detection and self correction on the machine agent side is also a way to solve this problem. High error sensitivity and good self correction capabilities of machine agent are helpful to reduce the correction cost caused by wrong decisions. There have been some studies using reinforcement learning (RL) to teach robots through real-time neural activities or error potential signal as feedback, and thus to enhance their abilities of error perception and correction (Ehrlich and Cheng 2018, Cheng *et al* 2020, Deng *et al* 2020).

Compared with the autonomy assistance in the picking process, the implementation of shared control in the placing process is rather thorny. This is because the position to be placed in real life is always decided by the users, and is unknown for the machine agent (unlike picking task with clear candidate goals). In our study, owing to height automatic adaptation, the system had a high tolerance for the false positive in the z axis. However, without the assistance of shared control, there were huge decreases of success rate and *TER* in the placing process compared with those in the picking process. Therefore, how to integrate machine intelligence and autonomous sensing technologies to better assist users during placement is a problem need to be considered carefully in the future.

4.3. Comparisons with the existing shared control methods

Recently, we have seen a great surge of shared control research in the BCI field. Most of the available shared control strategies manually set the arbitration coefficients (Li *et al* 2017, Muelling *et al* 2017, Xu *et al* 2019) or fusion rules (Sun *et al* 2019) according to the specific scenes, which impeded the transformative application of these approaches. In Zheng *et al* (2019) and Deng *et al* (2020), a recursive Bayesian model was also applied for arbitration, unfortunately, these methods directly fused the outputs of human and machine in probability, while did not consider the influence of actions on task decision-making during real-time control. Compared with other synchronous shared control methods, the fusion model in our study has two main advantages. Firstly, it utilized probabilistic fusion to optimize the corrected motion command while did not require to preset the rules based on the empiricism; secondly, the offline BCI performance of each subject and the real-time confidence score of inferred user's intention were taken into account in online control, guaranteeing the arbitration was indeed contextual: it dynamically allocated authorities depending on the individual characteristic and the actual control situation. Similar fusion concept was also reflected in (Deng *et al* 2020), which utilized a brain state evaluation network and motion prediction strategy to realize an adaptive control. The adopted reinforcement learning network in evaluated the BCI state of users in real time, which delivered a dynamic evaluation but more computational complexity was also introduced. In our study, we utilized hard coding of the simple subject's decoding accuracy to construct the human intention model. Although there was no real-time evaluation, the smaller computational complexity made it easier to deploy on the lightweight system. Different from using human

commands over a period of time to predict subject intent angle in Deng *et al* (2020), we inferred the user's intention according to the knowledge base of the machine agent and the current position, which led to the prediction more objective in shared control. In addition, it is worth noting that we utilized two-dimensional Gaussian distribution to model the motion of robotic arm, and then naturally extended the conventional planar shared control fusion to a 3D space.

4.4. Limitation and future work

Despite the superior performance of ADL with the shared control in this brain-actuated robotic arm system, there is still some work to be improved (except as mentioned in the previous section). The current GUI displayed stimuli and scene image feedback through a 21 inch, 60 Hz refresh rate displayer. The biggest difference between the video scene feedback and the real scene visual feedback is that the subjects can not perceive the depth information. In the actual experiment, we used a laser pen fixed at the end of the robotic arm to assist subjects to orient the robot. However, some subjects still reported that sometimes they felt confused about the scene image for a short time. Therefore integrating the GUI into a more immersive device (e.g. virtual reality devices) may have greater potential to enhance performance and increase the diversity of feedback. Although most of the subjects could complete the pick and place task with this system, there is still much room for improvement in decoding accuracy. Exploring the new cutting-edge BCI decoding algorithm will be expected to further improve the online performance of the system. Beyond that, combining the robot with other peripherals and expanding more functions are also important steps to realize the daily application of the brain-actuated system.

5. Conclusions

In this paper, a brain-actuated robotic arm system based on a novel shared control model with hybrid BCI scheme was proposed. Specifically, we built a shared controller which dynamically integrated the human intention with machine autonomy and intelligently optimized the robotic arm control process based on the actual control context. The adoption of the hybrid BCI scheme with SI and PI in this study aimed to extend the dimensionality of BCI control and optimize the BCI resources (e.g. decoding computing power, GUI occupation) for the system. The experiment results showed in the current system, all eleven subjects could pick the desired target from multiple objects under shared control and ten could complete the pick-place task. Moreover, the experiment results also demonstrated that shared control outperformed the pure BCI control, indicating shared control may be a promising method for brain-actuated systems.

Data availability statement

The data that support the findings of this study are available upon reasonable request from the authors.

Acknowledgments

We would like to thank all the researchers and subjects who have supported this study. This work was supported by the National Natural Science Foundation of China (Nos. 91848112, 61761166006) and the National Key Research and Development Program of China (No. 2018YFB1307301).

ORCID iDs

Linfeng Cao https://orcid.org/0000-0001-6930-115X
Guangye Li https://orcid.org/0000-0003-2530-3916

References

Bhattacharyya S, Konar A and Tibarewala D N 2014 A differential evolution based energy trajectory planner for artificial limb control using motor imagery EEG signal *Biomed. Signal Process. Control* **11** 107–13

Bi L, Fan X and Liu Y 2013 EEG-based brain-controlled mobile robots: a survey *IEEE Trans. Human-Machine Syst.* **43** 161–76

Blankertz B, Tomioka R, Lemm S, Kawanabe M and Muller K R 2007 Optimizing spatial filters for robust EEG single-trial analysis *IEEE Signal Process. Mag.* **25** 41–56

Chen X, Wang Y, Gao S, Jung T P and Gao X 2015a Filter bank canonical correlation analysis for implementing a high-speed SSVEP-based brain–computer interface *J. Neural Eng.* **12** 046008

Chen X, Wang Y, Nakanishi M, Gao X, Jung T P and Gao S 2015b High-speed spelling with a noninvasive brain–computer interface *Proc. Natl Acad. Sci.* **112** E6058–67

Chen X, Zhao B, Wang Y and Gao X 2019 Combination of high-frequency SSVEP-based BCI and computer vision for controlling a robotic arm *J. Neural Eng.* **16** 026012

Chen X, Zhao B, Wang Y, Xu S and Gao X 2018 Control of a 7-DOF robotic arm system with an SSVEP-based BCI *Int. J. Neural Syst.* **28** 1850018

Cheng G, Ehrlich S K, Lebedev M and Nicolelis M A L 2020 Neuroengineering challenges of fusing robotics and neuroscience *Sci. Robot.* **5** eabd1911

Combrisson E and Jerbi K 2015 Exceeding chance level by chance: the caveat of theoretical chance levels in brain signal classification and statistical assessment of decoding accuracy *J. Neurosci. Methods* **250** 126–36

Crandall J W and Goodrich M A 2002 Characterizing efficiency of human robot interaction: a case study of shared-control teleoperation *IEEE/RSJ Int. Conf. Intelligent Robots and Systems*

Daly J J and Wolpaw J R 2008 Brain–computer interfaces in neurological rehabilitation *Lancet Neurol.* **7** 1032–43

de Neeling M and Hulle M M V 2019 Single-paradigm and hybrid brain computing interfaces and their use by disabled patients *J. Neural Eng.* **16** 061001

Delorme A and Makeig S 2004 EEGLAB: an open source toolbox for analysis of single-trial EEG dynamics *J. Neurosci. Methods* **134** 9–12

Deng X, Yu Z L, Lin C, Gu Z and Li Y 2020 A Bayesian shared control approach for wheelchair robot with brain machine interface *IEEE Trans. Neural Syst. Rehabil. Eng.* **28** 328–38

Deng X, Yu Z L, Lin C, Gu Z and Li Y 2020 Self-adaptive shared control with brain state evaluation network for human-wheelchair cooperation *J. Neural Eng.* **17** 045005

Dragan A D and Srinivasa S S 2013 A policy-blending formalism for shared control *Int. J. Robot. Res.* **32** 790–805

Duan X, Xie S, Xie X, Meng Y and Xu Z 2019 Quadcopter flight control using a non-invasive multi-modal brain–computer interface *Front. Neurorobot.* **13** 23

Edelman B J, Meng J, Suma D, Zurn C, Nagarajan E, Baxter B S, Cline C C and He B 2019 Noninvasive neuroimaging enhances continuous neural tracking for robotic device control *Sci. Robot.* **4** eaaw6844

Ehrlich S K and Cheng G 2018 Human-agent co-adaptation using error-related potentials *J. Neural Eng.* **15** 066014

Flesher S N *et al* 2016 Intracortical microstimulation of human somatosensory cortex *Sci. Trans. Med.* **8** 361ra141–361ra141

Gao Q, Dou L, Belkacem A N and Chen C 2017 Noninvasive electroencephalogram based control of a robotic arm for writing task using hybrid BCI system *Biomed. Res. Int.* **2017** 8316485

Guger C, Ramoser H and Pfurtscheller G 2000 Real-time EEG analysis with subject-specific spatial patterns for a brain–computer interface BCI *IEEE Trans. Rehabil. Eng.* **8** 447–56

Guo H and Li Z 2008 Bayesian fusion theory and its application to the identification of structural damages *2008 Fourth Int. Conf. Natural Computation* pp 110–14

Han X, Lin K, Gao S and Gao X 2018 A novel system ofSSVEP-based human–robot coordination *J. Neural Eng.* **16** 016006

Hart S G and Staveland L E 1988 Development of NASA-TLX (task load index): results of empirical and theoretical research *Human Mental Workload* (*Advances in Psychology)* vol 52) ed P A Hancock and N Meshkati (Elsevier: Amsterdam) pp 139–83

He S *et al* 2020 EEG- and EOG-based asynchronous hybrid BCI: a system integrating a speller, a web browser, an e-mail client and a file explorer *IEEE Trans. Neural Syst. Rehabil. Eng.* **28** 519–30

Hochberg L R *et al* 2012 Reach and grasp by people with tetraplegia using a neurally controlled robotic arm *Nature* **485** 372–5

Iturrate I, Antelis J M, Kubler A and Minguez J 2009 A noninvasive brain-actuated wheelchair based on a P300 neurophysiological protocol and automated navigation *IEEE Trans. Robot.* **25** 614–27

Iturrate I, Chavarriaga R, Montesano L, Minguez J and Millán J 2015 Teaching brain-machine interfaces as an alternative paradigm to neuroprosthetics control *Sci. Rep.* **5** 13893

Johnson G D, Waytowich N R, Cox D J and Krusienski D J 2010 Extending the discrete selection capabilities of the P300 speller to goal-oriented robotic arm control *3rd IEEE RAS \& EMBS Int. Conf. on Biomedical Robotics and Biomechatronics* 572–5

Ke Y, Liu P, An X, Song X and Ming D 2020 An online SSVEP-BCI system in an optical see-through augmented reality environment *J. Neural Eng.* **17** 016066

Kim S K, Kirchner E A, Stefes A and Kirchner F 2017 Intrinsic interactive reinforcement learning-using error-related potentials for real world human–robot interaction *Sci. Rep.* **7** 17562

Kim Y J, Nam H S, Lee W H, Seo H G, Leigh J H, Oh B M, Bang M S and Kim S 2019 Vision-aided brain–machine interface training system for robotic arm control and clinical application on two patients with cervical spinal cord injury *Biomed. Eng. Online* **18** 14

Kim Y J, Park S W, Yeom H G, Bang M S, Kim J S, Chung C K and Kim S 2015 A study on a robot arm driven by three-dimensional trajectories predicted from non-invasive neural signals *Biomed. Eng. Online* **14** 81

Li G and Zhang D 2016 Brain–computer interface controlled cyborg: establishing a functional information transfer pathway from human brain to cockroach brain *PLoS One* **11** 1–17

Li Y, Long J, Yu T, Yu Z, Wang C, Zhang H and Guan C 2010 An EEG-based BCI system for 2-D cursor control by combining mu/beta rhythm and P300 potential *IEEE Trans. Biomed. Eng.* **57** 2495–505

Li Z, Zhao S, Duan J, Su C, Yang C and Zhao X 2017 Human cooperative wheelchair with brain–machine interaction based on shared control strategy *IEEE/ASME Trans. Mechatron.* **22** 185–95

Lin Z, Zhang C, Zeng Y, Tong L and Yan B 2018 A novel P300 BCI speller based on the triple RSVP paradigm *Sci. Rep.* **8** 3350

Long J, Li Y, Yu T and Gu Z 2011 Target selection with hybrid feature for BCI-based 2-D cursor control *IEEE Trans. Biomed. Eng.* **59** 132–40

Long J, Shelhamer E and Darrell T 2015 Fully convolutional networks for semantic segmentation *2015 Conf. Computer Vision and Pattern Recognition (CVPR)* pp 3431–40

Ma T *et al* 2017 The hybridBCI system for movement control by combining motor imagery and moving onset visual evoked potential *J. Neural Eng.* **14** 026015

Martinez P, Bakardjian H and Cichocki A 2007 Fully online multicommand brain–computer interface with visual neurofeedback using SSVEP paradigm *Computat. Intell. Neurosci.* **2007** 094561

McGeady C, Vučković A and Puthusserypady S 2019 A hybridMI-SSVEP based brain computer interface for potential upper limb neurorehabilitation: a pilot study *2019 7th Int. Conf. on Brain–Computer Interface (BCI)* pp 1–6

Meng J, Zhang S, Bekyo A, Olsoe J, Baxter B and He B 2016 Noninvasive electroencephalogram based control of a robotic arm for reach and grasp tasks *Sci. Rep.* **6** 38565

Muelling K *et al* 2017 Autonomy infused teleoperation with application to brain computer interface controlled manipulation *Auton. Robots* **41** 1401–22

Onose G *et al* 2012 On the feasibility of using motor imagery EEG-based brain–computer interface in chronic tetraplegics for assistive robotic arm control: a clinical test and long-term post-trial follow-up *Spinal Cord* **50** 599–608

Pathirage I, Khokar K, Klay E, Alqasemi R and Dubey R 2013 A vision based P300 brain–computer interface for grasping using a wheelchair-mounted robotic arm *2013 IEEE/ASME Int. Conf. Advanced Intelligent Mechatronics* pp 188–93

Perera C J, Naotunna I, Sadaruwan C, Gopura R A R C and Lalitharatne T D 2016 SSVEP based BMI for a meal assistance robot *2016 IEEE Int. Conf. Systems, Man and Cybernetics (SMC)* pp 002295–300

Pfurtscheller G and Lopes da Silva F 1999 Event-related EEG/MEG synchronization and desynchronization: basic principles *Clin. Neurophysiol.* **110** 1842–57

Pinheiro O R, Alves L R G and Souza J R D 2018 EEG signals classification: motor imagery for driving an intelligent wheelchair *IEEE Latin Am. Trans.* **16** 254–9

Rakshit A, Lahiri R, Ghosal S, Sarkar A, Ghosh S and Konar A 2016 Robotic link position control using brain computer interface *2016 Int. Conf. Microelectronics, Computing and Communications (MicroCom)* pp 1–6

Russell B C, Torralba A, Murphy K P and Freeman W T 2008 Labelme: a database and web-based tool for image annotation *Int. J. Comput. Vis.* **77** 157–73

Rusu R B and Cousins S 2011 3D is here: Point cloud library (PCL) *2011 IEEE Int. Conf. Robotics and Automation* pp 1–4

Salazar-Gomez A F, DelPreto J, Gil S, Guenther F H and Rus D 2017 Correcting robot mistakes in real time using EEG signals *2017 IEEE Int. Conf. Robotics and Automation (ICRA)* pp 6570–7

Sellers E W, Krusienski D J, McFarland D J, Vaughan T M and Wolpaw J R 2006 A P300 event-related potential brain–computer interface BCI: the effects of matrix size and inter stimulus interval on performance *Biol. Psychol.* **73** 242–52

Sun F, Zhang W, Chen J, Wu H, Tan C and Su W 2019 Fused fuzzy petri nets: a shared control method for brain–computer interface systems *IEEE Trans. Cogn. Dev. Syst.* **11** 188–99

Sutter E E 1992 The brain response interface: communication through visually-induced electrical brain responses *J. Microcomput. Appl.* **15** 31–45

Tanaka K, Matsunaga K and Wang O 2005 Electroencephalogram-based control of an electric wheelchair *IEEE Trans. Robot.* **21** 762–6

Vallabhaneni A, Wang T and He B 2005 *Brain—Computer Interface* (Boston, MA: Springer) pp 85–121

Wang M, Daly I, Allison B Z, Jin J, Zhang Y, Chen L and Wang X 2015 A new hybrid BCI paradigm based on P300 and SSVEP *J. Neurosci. Methods* **244** 16–25 Brain Computer Interfaces; Tribute to Greg A Gerhardt

Wang M, Li R, Zhang R, Li G and Zhang D 2018 A wearableSSVEP-based BCI system for quadcopter control using head-mounted device *IEEE Access* **6** 26789–98

Wu J S, Zheng W S and Lai J H 2013 Euler clustering *Proc. of the 23rd Int. Joint Conf. on Artificial Intelligence* (IJCAI/AAAI) pp 1792–8

Xu Y, Ding C, Shu X, Gui K, Bezsudnova Y, Sheng X and Zhang D 2019 Shared control of a robotic arm using non-invasivebrain–computer interface and computer vision guidance *Robot. Auton. Syst.* **115** 121–9

Xu Y, Zhang H, Cao L, Shu X and Zhang D 2020 A shared control strategy for reach and grasp of multiple objects using robot vision and noninvasive brain–computer interface *IEEE Trans. Autom. Sci. Eng.* 1–13

Yan N, Wang C, Tao Y, Li J, Zhang K, Chen T, Yuan Z, Yan X and Wang G 2020 Quadcopter control system using a hybrid BCI based on off-line optimization and enhanced human-machine interaction *IEEE Access* **8** 1160–72

Yao L, Sheng X, Zhang D, Jiang N, Mrachacz-Kersting N, Zhu X and Farina D 2017 A stimulus-independent hybrid BCI based on motor imagery and somatosensory attentional orientation *IEEE Trans. Neural Syst. Rehabil. Eng.* **25** 1674–82

Yu T, Xiao J, Wang F, Zhang R, Gu Z, Cichocki A and Li Y 2015 Enhanced motor imagery training using a hybrid BCI with feedback *IEEE Trans. Biomed. Eng.* **62** 1706–17

Zheng W, Liu Q, Chen K, Ai Q, Meng W and Shi Z 2019 Brain-robot shared control based on motor imagery and improved Bayes filter *2019 IEEE/ASME Int. Conf. Advanced Intelligent Mechatronics (AIM)* pp 139–44

Ziebart B D, Maas A, Bagnell J A and Dey A K 2008 Maximum entropy inverse reinforcement learning *Proc. 23rd Conf. Artificial Intelligence* vol 3 (AAAI Press) pp 1433–8